submitted to *Geophys. J. Int.*

Supplementary Material "A Reduced Order Approach for Probabilistic Inversions of 3D Magnetotelluric Data I: General Formulation"

1 BENCHMARKS *MAX3D-G*

The problems presented and discussed in this section represent typical benchmarks found in the literature aiming at comparing solutions of the MT forward problem as well as to assess the computational efficiency of different algorithms. Here the particular interest is comparing our new implementation (hereafter referred to as *Max3D-G*) against the original *Max3D* algorithm with Domain Decomposition (hereafter referred to as *Max3D*-DDC) developed by Zyserman & Santos (2000). The performance of these algorithms relative to some other popular codes is also discussed. Additional benchmarks of the original code, *Max3D*-DDC, can be found in Zyserman & Santos (2000).

1.1 DTM1 Model

In 2008, a 3D-MT inversion and modeling workshop was held at the Dublin Institute for Advanced Studies with the aim of discussing and assessing the state of 3D modeling in magnetotellurics. In order to compare the forward and inversion solutions from different codes, several electrical conductivity models were proposed. The reader is referred to the review of this workshop by Miensopust et al. (2013) for details on the proposed models and obtained results. Of all the proposed models, the DTM1 model was specifically developed to show how different codes deal with strong resistivity contrasts. It consists of three blocks of different conductivity (10, 1 and 10000 Ωm) inside an homogeneous 100 Ωm semi-space. Figure S1 shows a description of the blocks and a plan view of the model. The origin of coordinates is placed at the center of body 1. Figure S2 shows two vertical slices of the model for different northing profiles.

In what follows, we compare the results and computation times for the DTM1 model for various

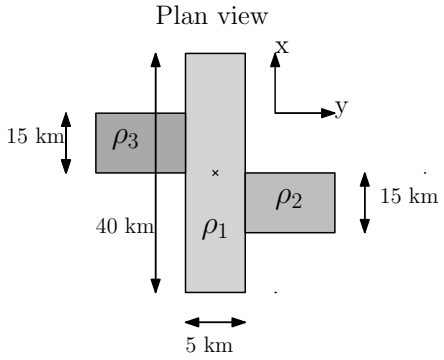

	x (km)	y (km)	z (km)	resistivity (ohm.m)
body 1	-20 to 20	-2.5 to 2.5	5 to 20	10
body 2	-15 to 0	-2.5 to 22.5	20 to 25	1
body 3	0 to 15	-22.5 to 2.5	20 to 50	10000
background				100

Figure S1. Plan view of DTM1 model. The symbol × indicates the origin of coordinates

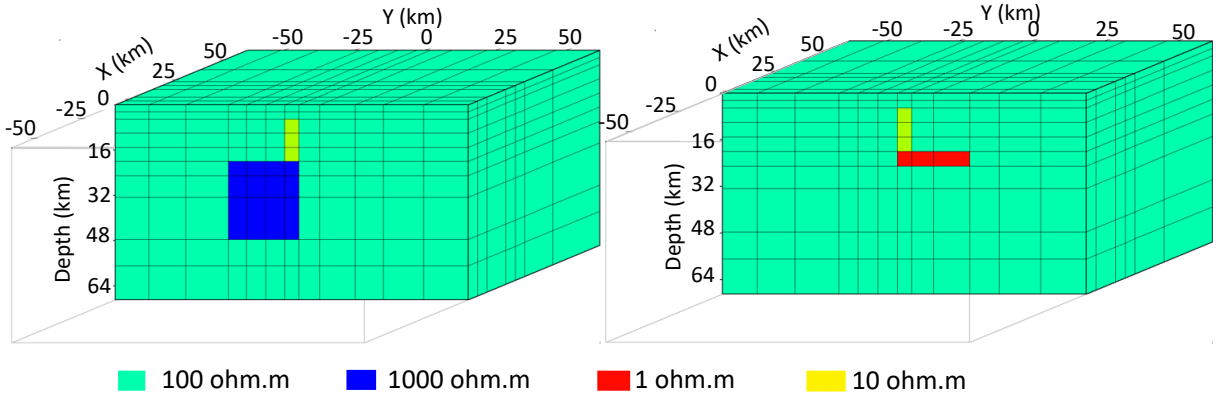

Figure S2. Different side views of the DTM1 model illustrating the three anomalies embedded in a 100 background.

codes including *Max3D*-DDC and *Max3D-G*. The results obtained with each code depend on the mathematical formulation, its numerical approximation (i.e., finite differences, integral equation or finite elements), the discretization of the domain, the coordinate system and how boundary conditions are implemented.

For our comparison we use the 3D forward responses provided by Prof. Alan Jones in his MTnet website ⋆ computed by different users of the following codes:

(1) The FE code of Myung Jin Nam (Nam et al., 2007) used by Nuree Han and Tae Jong Lee.
(2) *WinGLink* FD code (Mackie et al., 1994) used by Randy Mackie and Marion Miensopust.
(3) *Wsinv3dmt* FD code (Siripunvaraporn et al., 2002) used by Marion Miensopust.
(4) *Mt3dinv* FD code (Farquharson et al., 2002) used by Marion Miensopust.

⋆ http://www.mtnet.info/main/

The forward responses were computed for a period range of 0.1s to 10^4s at four periods per decade (21 periods) along 4 profiles with 5 km site spacing: profiles at $x = -15, 0, 15$ km between $y = -37.5$ km and $y = 37.5$ km and a profile at $y = 0$ between $x = -25$ km and $x = 25$ km. We follow the same procedure to compute our responses using *Max3D-DDC* and our new implementation *Max3D-G*.

For *Max3D-DDC* we used a model of $26 \times 26 \times 17$ elements plus one layer of air with resistivity $\rho = 1e^{15}$ Ωm. The layered 1D background is comprised of four layers and a semi-space of resistivity $\rho = 100$ Ωm. We computed the forward responses with 117 processors, obtaining the solution in 50.62 seconds. For *Max3D-G* and using the same model, we performed the computations with 2 processors per frequency to solve the linear system of equations using MUMPS and obtained the solution in 10.11 seconds.

Figures S4 and S3 show the apparent resistivity and phase of the impedance components computed with *Max3D-DDC* along two profiles located at $x = 0$ and $y = 0$ for 1000 s and along a profile located at $x = 15$ km for 1000 s, respectively. Figures S6 and S5 show the apparent resistivity and phase computed with *Max3D-G* along the same profiles and periods. In all figures we include the results obtained with the codes (1)-(4). Table S7 extracted from Miensopust et al. (2013) lists the forward results obtained with the codes used at the workshop. With the aim of a comparison amongst the different approaches we have also included our results.

The results obtained with *Max3D*-DDC and *Max3D-G* are in excellent agreement with those predicted by the other tested algorithms. In particular, the results show that the responses for *Max3D-G* and *Max3D-DDC* are, in practice, identical, and that when using *Max3D-G*, we obtain time reductions of 80% with only 30% of the processors. We also observe a significant reduction in computational time when using *Max3D*-DDC and *Max3D-G* (Table S7) compared to the rest of the tested algorithms. This is because the use of absorbent boundary conditions (Sheen, 1997) and a secondary field formulation allow us to obtain accurate solutions while keeping the size of the numerical domain smaller than that needed in other formulations, and, therefore, reducing the computational time.

1.2 Model 2

Here we present a comparison of the forward responses predicted by *ModEM* (Egbert & Kelbert, 2012), *Max3D*-DCC and our new implementation, *Max3D-G*.

The model used comprises three blocks of 2000 Ωm, 5 Ωm and 40 Ωm, respectively, embedded in an homogeneous semi-space of 100 Ωm. Figure S8 describes the coordinate system, location and dimensions of the blocks.

Forward responses were calculated for a period range of 1s to 10^4s, with seven periods per decade

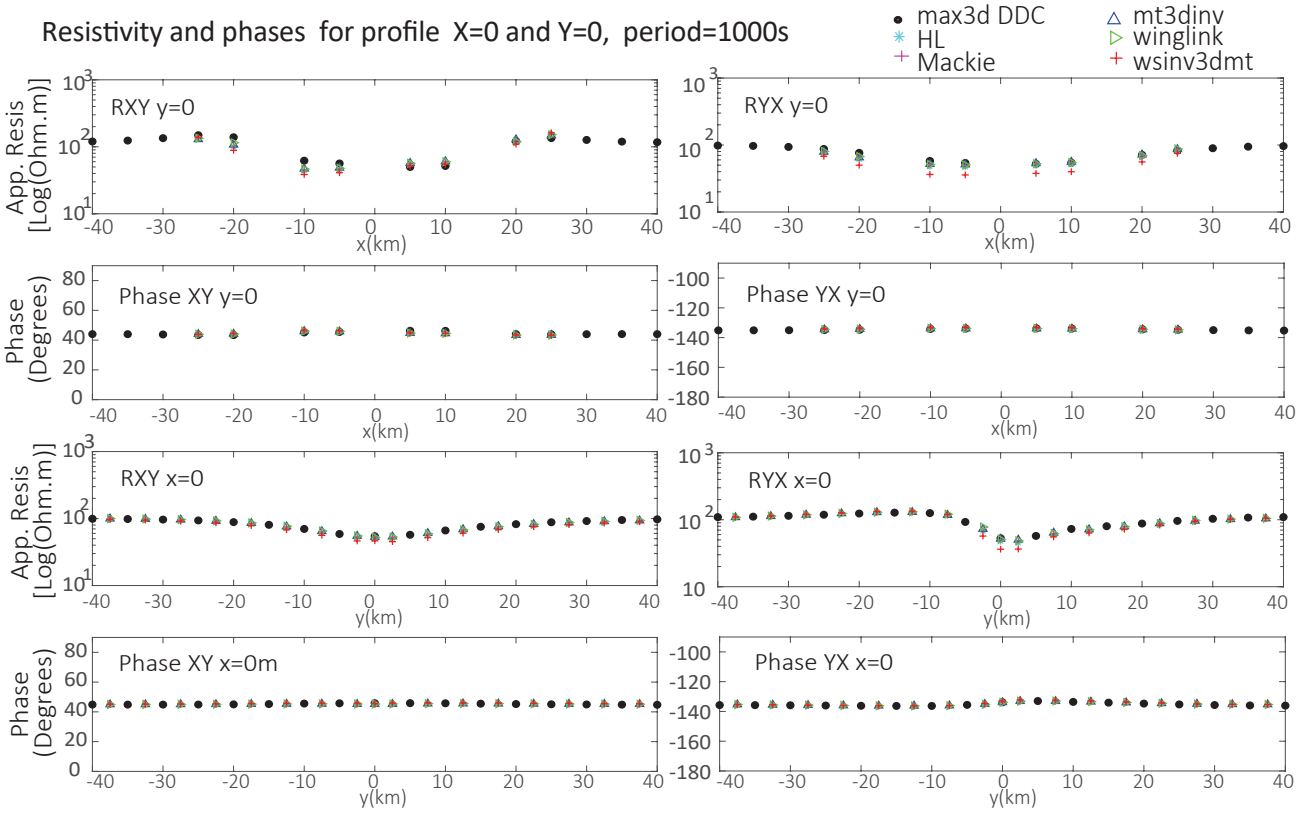

Figure S3. Apparent resistivity and phase derived from the off-diagonal elements of the impedance tensor at profiles $x = 0$ and $y = 0$ for 1000 s. We use *Max3D-DDC* and other codes referred to as: *HL* (Nam et al., 2007), *Mackie* (Mackie et al., 1994), *winGLink* (Mackie et al., 1994), *wsinv3dmt* (Siripunvaraporn et al., 2002) and *mt3dinv* (Farquharson et al., 2002).

(29 periods), at 2500 sites located between -125 km and 125 km in both directions (x and y). The spacing between stations was set to 5 km. Figure S9 shows a side view of the model.

The numerical model used to compute the responses with *ModEM* was 1216 km × 1216 km × 1092 km, discretized with $74 \times 74 \times 50$ cells. The computation was done using the control parameters of Table S1.

Table S1: Control parameters used for the ModEM inversion

Number of QMR iters per divergence correction	40
Maximum number of divergence correction calls	20
Maximum number of divergence correction iters	100
Misfit tolerance for EM forward solver	1.0 e^{-7}
Misfit tolerance for EM adjoint solver	1.0 e^{-7}
Misfit tolerance for divergence correction	1.0 e^{-5}

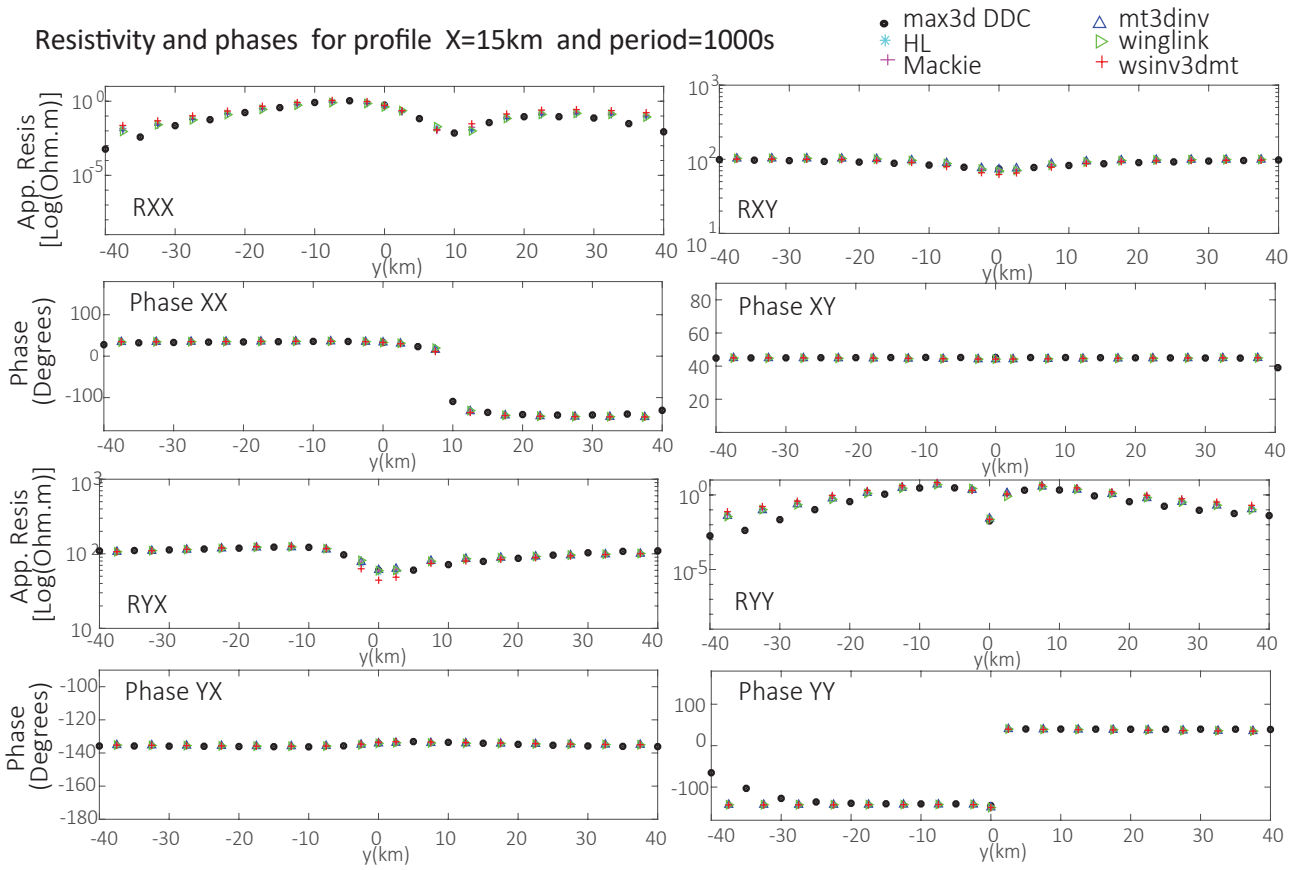

Figure S4. Apparent resistivity and phase derived from all elements of the impedance tensor at profile $x = 15$ km and period of 1000 s. We use *Max3D-DDC* and other codes referred to as: *HL* (Nam et al., 2007), *Mackie* (Mackie et al., 1994), *winGLink* (Mackie et al., 1994), *wsinv3dmt* (Siripunvaraporn et al., 2002) and *mt3dinv* (Farquharson et al., 2002).

The solution was obtained in 163 seconds using 50 processors Xeon(R) CPU E5-2680 @2.70GHz. The time increased to 198 seconds when using 64 processors.

In order to study the advantages of the absorbent boundary conditions in terms of the domain size and associated reduction in computational time, we used a model of considerably smaller size for both implementations of *Max3D*: 250 $km \times 250\ km \times 180\ km$ and $50 \times 50 \times 40$ cells. The background model included one air layer of resistivity $\rho = 1e^{15}\ \Omega m$ and four 1D layers plus a semi-space of resistivity $\rho = 100\ \Omega m$. The computation for the 29 periods using *Max3D*-DCC took 665.8 seconds using 50 processors Xeon(R) CPU E5-2680 @2.70GHz, whereas *Max3D-G* solved the problem in 44 seconds using 12 processors per frequency and 158 seconds using 4 processors per frequency.

Figures S10 and S11 show a comparison of the apparent resistivity and phase derived from the off-diagonals components of the impedance tensor computed with *Max3D-DCC* and *ModEM*. The same comparison, but now between *Max3D-G* and *ModEM*, is shown in Figures S12 and S13. The

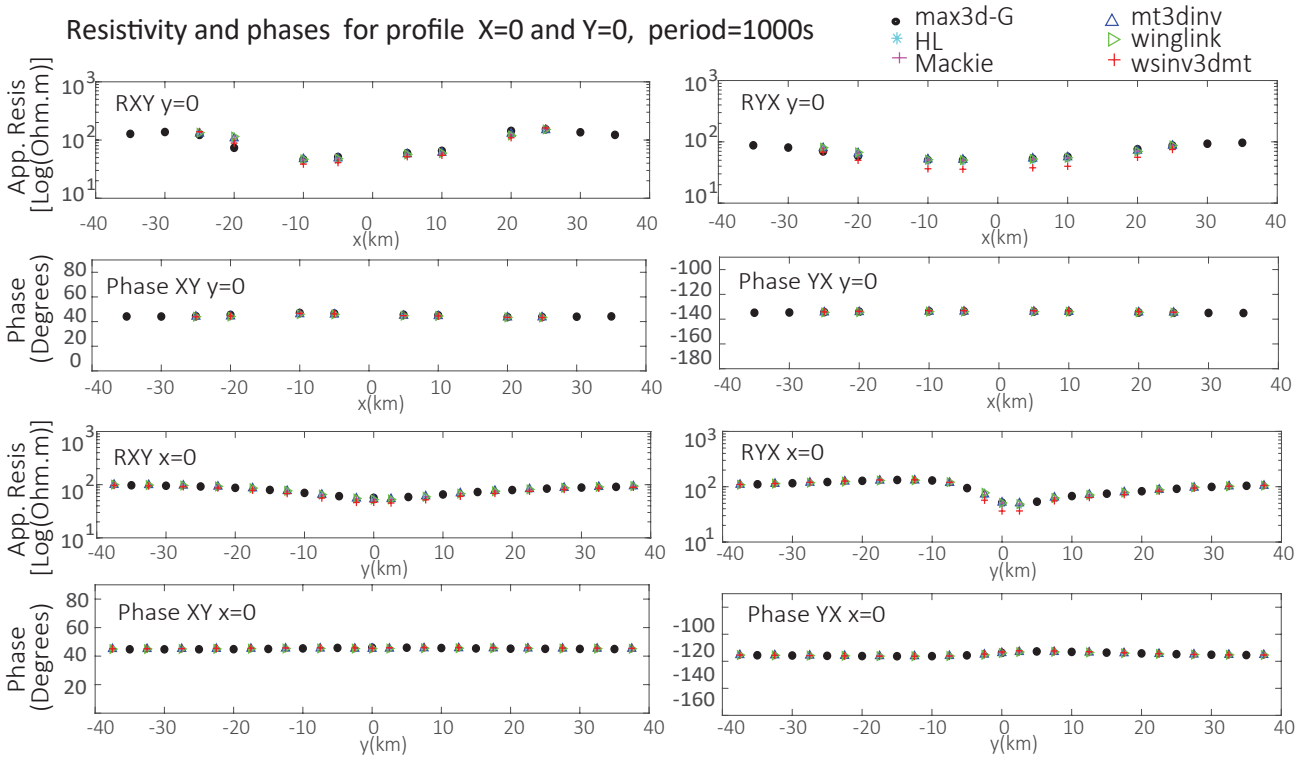

Figure S5. Apparent resistivity and phase derived from the off-diagonal elements of the impedance tensor at profiles $x = 0$ and $y = 0$ for 1000 s. We use *Max3D-G* and other codes referred to as: *HL* (Nam et al., 2007), *Mackie* (Mackie et al., 1994), *winGLink* (Mackie et al., 1994), *wsinv3dmt* (Siripunvaraporn et al., 2002) and *mt3dinv* (Farquharson et al., 2002).

responses are plotted for the 50 cells placed at the centre of the model between -125 km to 125 km at $x = 0$ and for all the 29 frequencies (vertical axis). The first frequency (top of y axis) is the period 1s and the 29th (bottom of y axis) is the period 10^4s.

The responses of *Max3D-G* and *Max3D-DCC* are, for all practical purposes, identical. The minor differences are mostly due to the iterative process of *Max3D-DCC* and associated convergence tolerance. The responses predicted by all three codes (*Max3D-G*, *Max3D*-DCC, *ModEM*) agree well with each other. Some minor differences are observed in the phase and apparent resistivity at periods higher than 100s (freq $n°15$ in the figures) and 1000s (freq $n°22$ in the figures), respectively, where *ModEM* shows higher values in the phase of Z_{xy} and Z_{yx} and lower apparent resistivity for the Z_{xy} component. Both *Max3D-G* and *Max3D*-DCC, introduce a small boundary effect associated with the smaller size of the domain. This effect can be seen in the right and left border (cell $n°1$ and $n°50$) of panels (a) of Figs.S10 and S11. It can be also noted that although the numerical domain used for *ModEM* was considerably larger than that used for *Max3D* a boundary effect seems to be present in the *ModEM* responses for low frequencies. This possible boundary effect can be observed for period

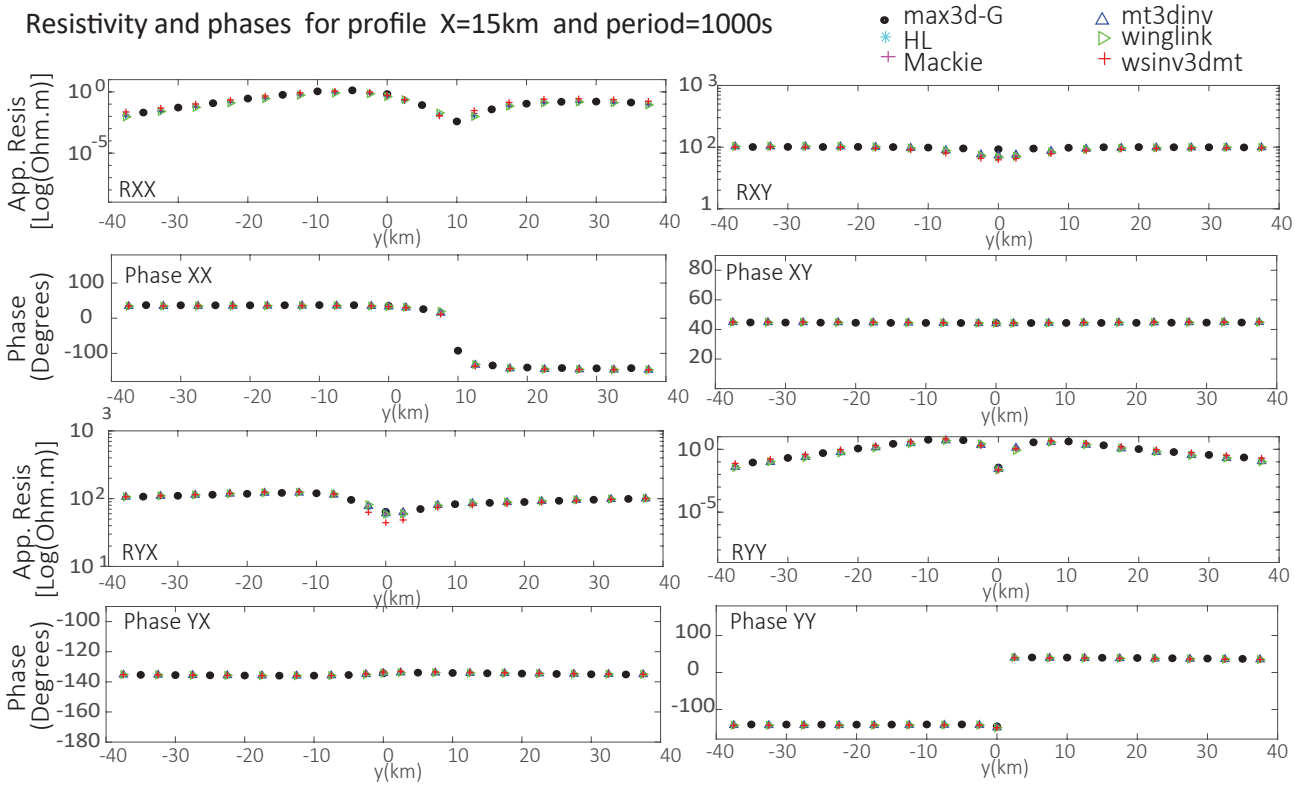

Figure S6. Apparent resistivity and phase derived from all elements of the impedance tensor at profile $x = 15$ km for 1000s. We use *Max3D-G* and other codes referred to as: *HL*(Nam et al., 2007), *Mackie* (Mackie et al., 1994), *winGLink* (Mackie et al., 1994), *wsinv3dmt* (Siripunvaraporn et al., 2002) and *mt3dinv* (Farquharson et al., 2002).

10000s in apparent resistivities (freq $n°29$, bottom of panels (c) and (d) of Figs.S10 and S12) and for periods higher than 3727s (freq $n°27$, bottom of panels (c) and (d) of Figs.S11 and S13). It is unclear if this effect may be the reason for the differences observed at high periods or if *ModEM* exhibits higher sensitivity to the deeper conductive block than *Max3D*-DCC and *Max3D-G*.

In an attempt to clarify these differences, Figure S14 shows the subtraction of apparent resistivity and phase computed with *Max3D-G* from the responses computed with *ModEM*. The differences are less than 6 Ωm in apparent resistivity and 1 degree in phase, displaying the aforementioned sensitivity of *ModEM*. The small numerical boundary effect introduced by *Max3D-G* and *Max3D*-DCC, and the possible boundary effect in the *ModEM* responses are also notable. Given the similar results between *Max3D-G* and *ModEM* together with the considerable computational time difference (163 seconds against 44 seconds) and the excellent performance of the absorbent boundaries conditions we adopt our implementation *Max3D-G* for the work that follows and our probabilistic inversion framework.

Code	User	Mesh (number of cells)	CPU time and tolerance AT/TT	Computer used
FD (Egbert & Kelbert, 2012)	Naser Meqbel	$42 \times 42 \times 56$ (plus 10 air layers)	–	–
FD (Farquharson et al., 2002)	Colin Farquharson	$72 \times 72 \times 72$ (2.5 km)	AT: $10^{-8}$to 10^{-10} (low tolerance for long period)	Mac PowerPC G5, 2GHz
(serial)	Elliot Holtham	$> 1s : 44 \times 52 \times 43$ (2.5 km)	49 h 37 min TT: 10^{-9} (not achieved at all periods)	Dual AMD 244 Opteron CPU 4GB RAM
(frequency parallelization)	Doug Oldenburg	≤ 1 s: $104 \times 114 \times 46$ (0.5 km)		
(serial)	Marion Miensopust	$92 \times 58 \times 37$ (0.51 km)	–	–
FD (Mackie et al., 1994)	Randall Mackie	$95 \times 95 \times 73$	30 min TT: 10^{-10}	36 Dual processor Xeons, 3.2 GHz
(parallelization with PETSc distributes linear system /not exactly domain decomposition)		(without air layers)		
(serial)	Marion Miensopust	$85 \times 62 \times 34$ (plus 10 air layers)	51 min TT:10^{-8}	Intel Core2 CPU E6300, 1.86 GHz,3.25GB RAM
FD (Newman & Alumbaugh, 2000)	Greg Newman	$285 \times 207 \times 125$ (0.3 km)	4 min - 38 min /period	Parallel Linux cluster
(frequency parallelization and domain decomposition; see reference)		to $161 \times 171 \times 145$ (1 km)	TT:10^{-12}	using 64 cores
FD (Sasaki, 2001)	Yutaka Sasaki	$65 \times 83 \times 51$	1 h 14 min	Pentium 4PC, 2GB RAM
FD (Siripunvaraporn et al., 2002)	Marion Miensopust	$39 \times 40 \times 18$ (1-2.5 km)	1 h 18 min	Intel Core2 CPU E6300,
(serial)		(plus 7 air layers)	TT: 10^{-7}	1.86 GHz, 3.25GB RAM
FE (Nam et al., 2007)	Nuree Han and Tae Jong Lee	$48 \times 47 \times 31$	57 h 16 min	256 nodes IBM x335, 2CPUs each (Pentium IV Xeon DP 2.8 GHz)
IE (Avdeev et al., 2002)	Dmitry Avdeev	$120 \times 135 \times 23$	4 h 11 min	Laptop: T7200 2GHz CPU, 2GB RAM
FE Max3D (Zyserman & Santos, 2000)	Constanza Manassero	$26 \times 26 \times 18$ (2.5 km)	50.62 sec	Xeon(R) E5-26800 2.70GHz CPU
(domain decomposition)		(1 air layer)	(21 frequencies)	117 processors
FE Max3D-G	Constanza Manassero	$26 \times 26 \times 18$ (2.5 km)	10.11 sec	Xeon(R) E5-26800 2.70GHz CPU
(frequency parallelization and parallelization with MUMPS for solving linear system)		(1 air layer)	(21 frequencies)	(2 CPU per frequency)

Figure S7. List of DTM1 forward results extracted from Miensopust et al. (2013) and modified to include our results. The table specifies: code and its type (FD, FE or IE), user, mesh and in parentheses (if available) the lateral width of the cells at the centre of the model, required CPU time (and target tolerance TT or achieved tolerance AT) and computer used.

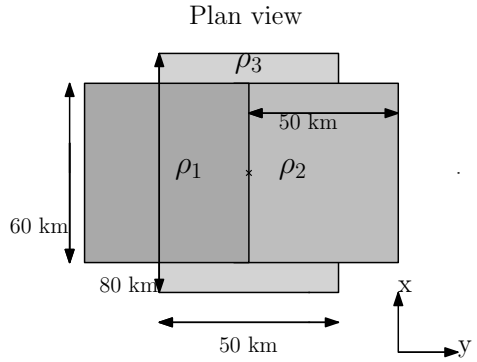

	x (km)	y (km)	z (km)	resistivity (ohm.m)
body 1	-30 to 30	-50 to 0	33 to 65	2000
body 2	-30 to 30	0 to 50	33 to 65	5
body 3	-40 to 40	-25 to 25	107 to 150	40
background				100

[ht]

Figure S8. Plan view Model 2. The symbol $\times$ indicates the origin of coordinates.

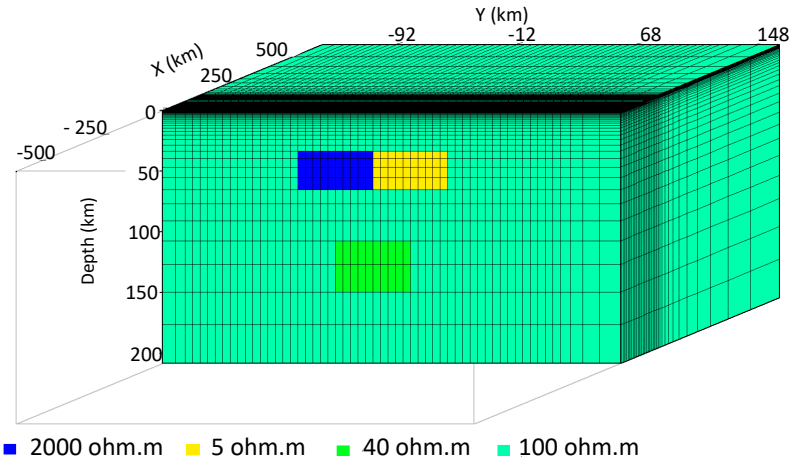

Figure S9. Side view Model 2 showing three anomalies embedded in a 100 background.

2 AN ILLUSTRATIVE APPLICATION OF THE RB+MCMC ALGORITHM: 1D HEAT-TRANSFER PROBLEM

In this section, we illustrate the basic features of the RB+MCMC algorithm with a simple and familiar 1D heat transfer problem. This allows us to compute the exact posterior PDFs using high-fidelity numerical models that we can use to compare with the approximations from our method.

2.1 Model setup

The forward problem involves the calculation of 1D geotherms for a two-layer (crust plus lithospheric mantle) lithospheric model by solving the 1D steady-state equation

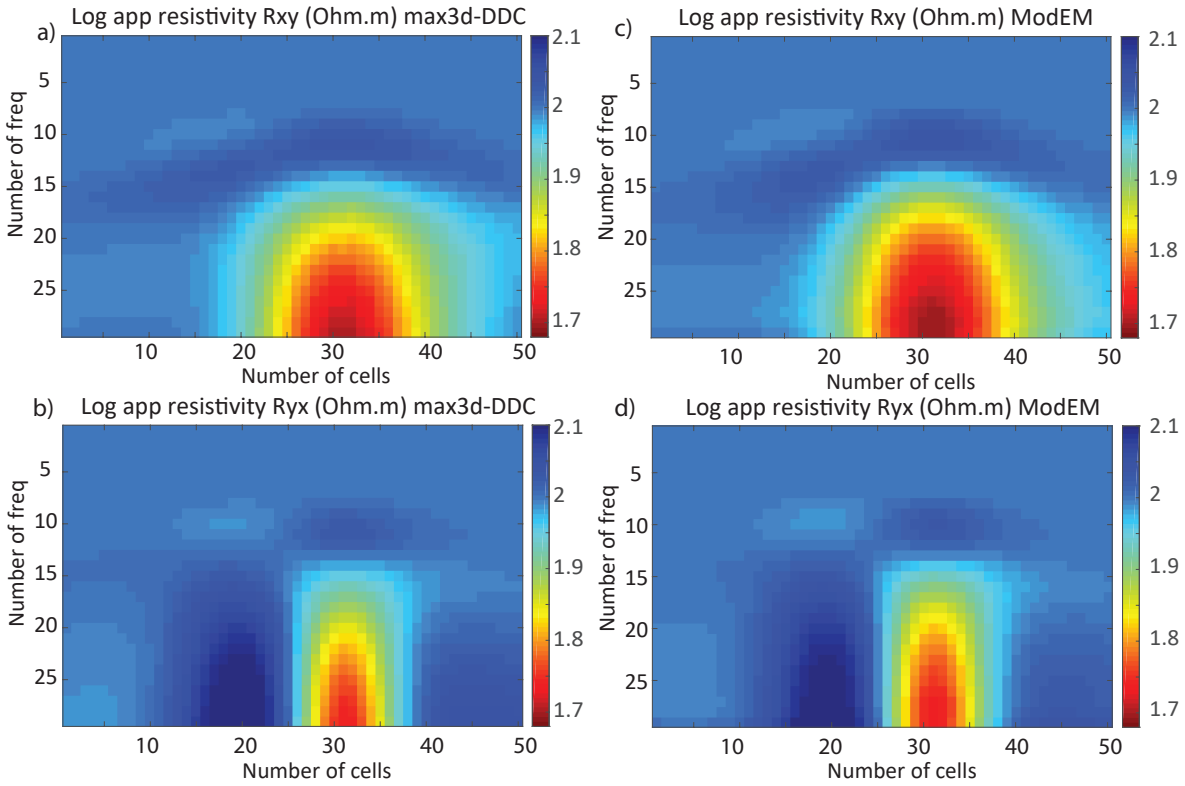

Figure S10. Apparent resistivity derived from the off-diagonals components of the impedance tensor computed with (a)-(b) *Max3D-DDC* and (c)-(d) ModEM. (a)-(d) Plots for 50 cells between -125 km to 125 km at $x = 0$ and for 29 frequencies (vertical axes) between 1 s and 10^4 s.

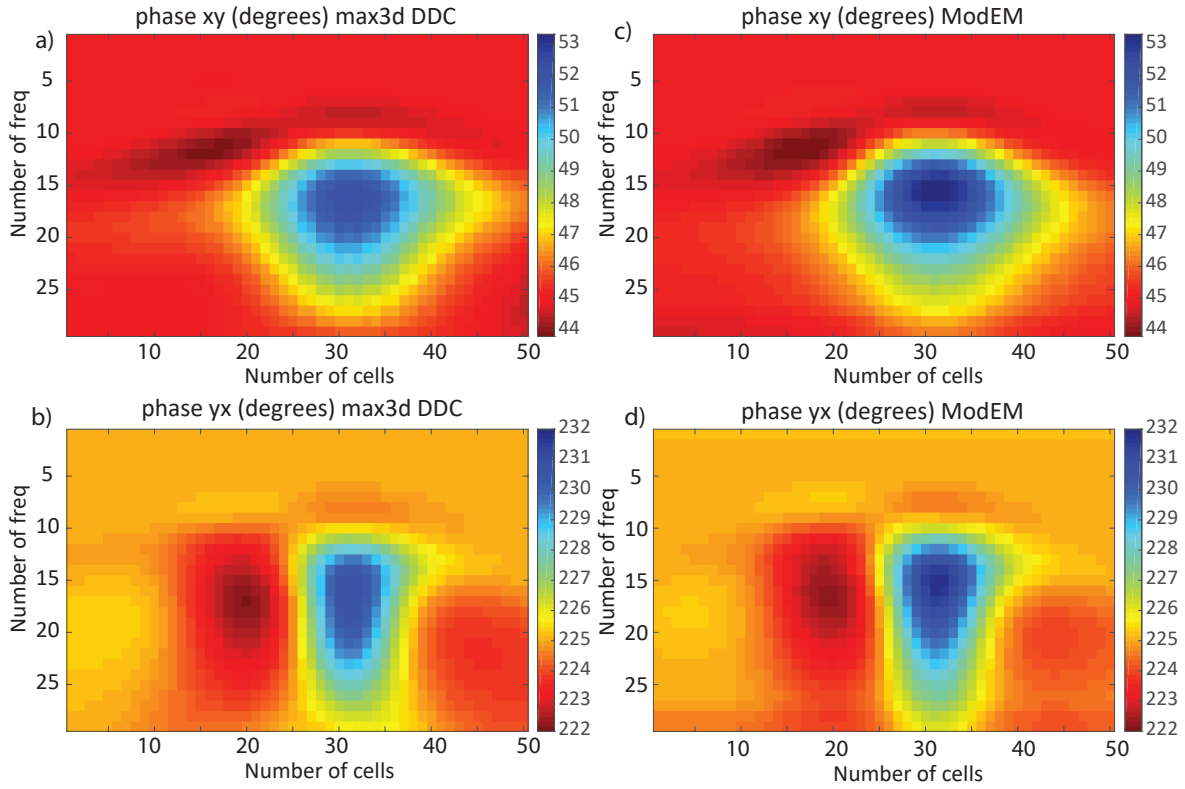

Figure S11. Apparent phase derived from the off-diagonal components of the impedance tensor computed with (a)-(b) *Max3D-DDC* and (c)-(d) ModEM. (a)-(d) Plots for 50 cells between -125 km to 125 km at $x = 0$ and for 29 frequencies (vertical axes) between 1s and 10^4s.

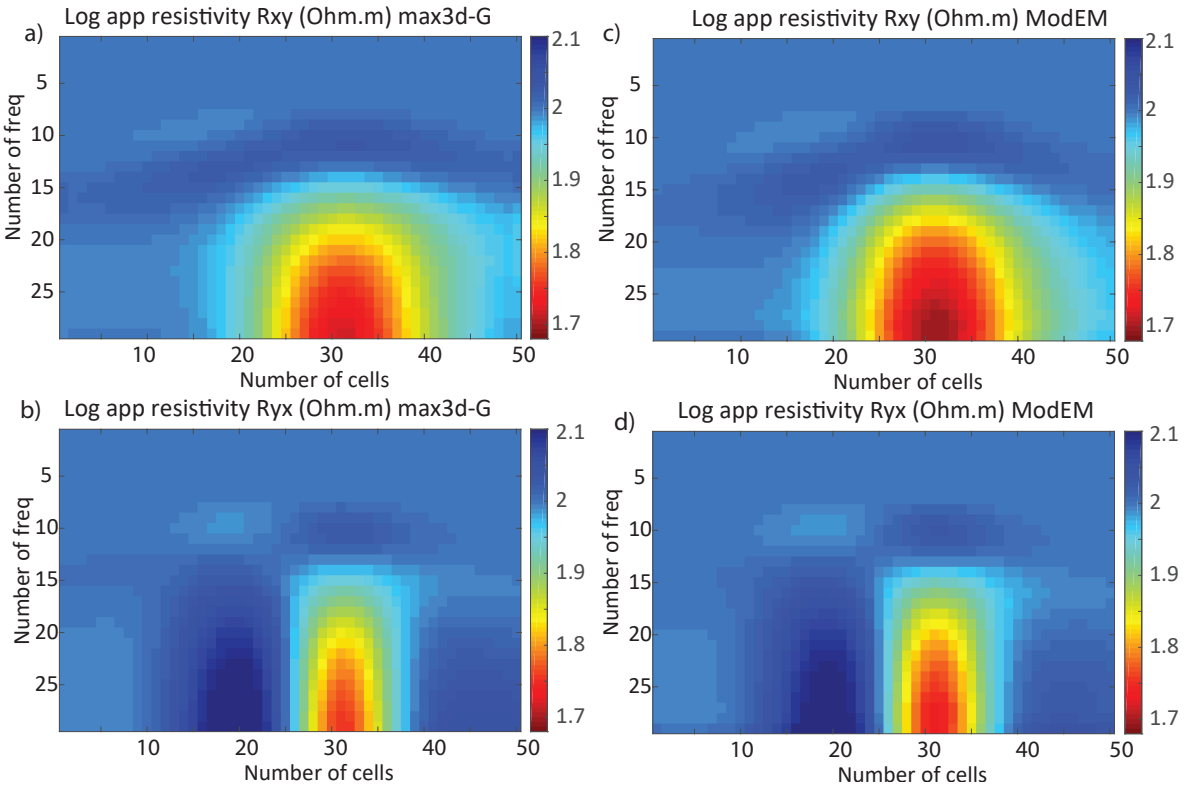

Figure S12. Apparent resistivity derived from the off-diagonal components of the impedance tensor computed with (a)-(b) *Max3D-G* and (c)-(d) ModEM. (a)-(d) Plots for 50 cells between -125 km to 125 km at $x = 0$ and for 29 frequencies (vertical axes) between 1s and 10^4s.

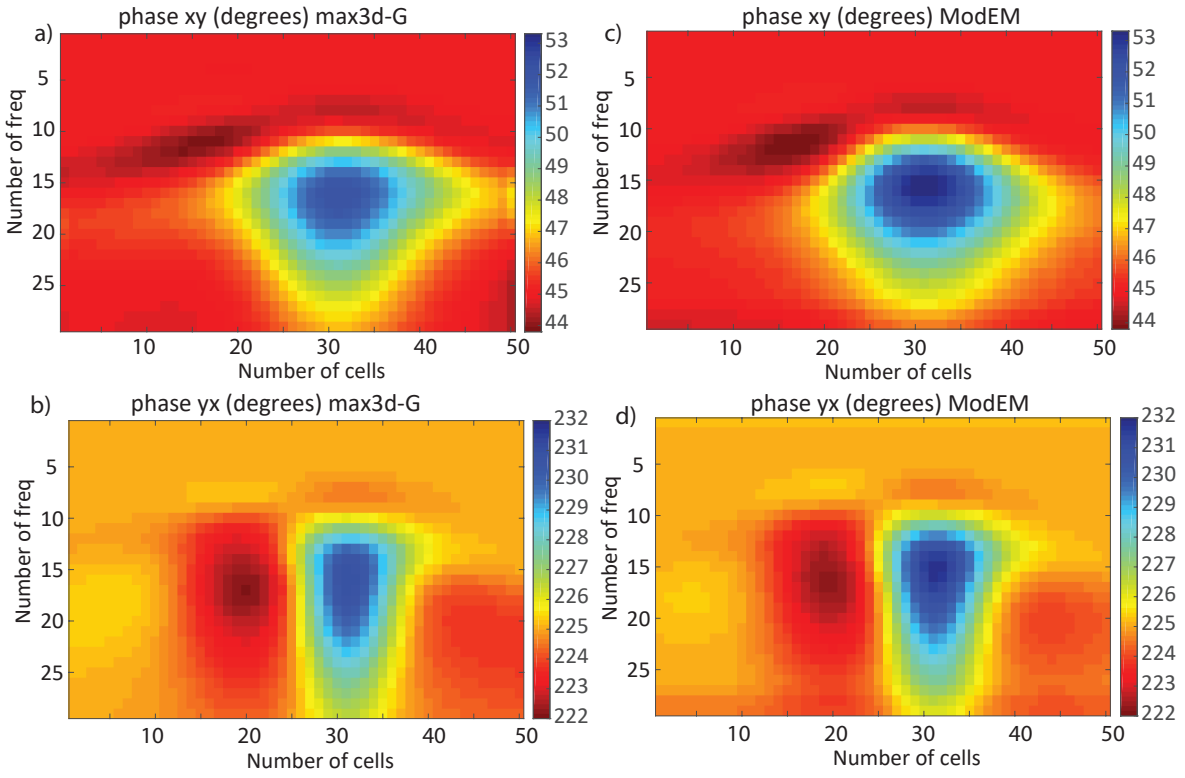

Figure S13. Apparent phase derived from the off-diagonals components of the impedance tensor computed with (a)-(b) *Max3D-G* and (c)-(d) ModEM. (a)-(d) Plots for 50 cells between -125 km to 125 km at $x = 0$ and for 29 frequencies (vertical axes) between 1s and 10^4s.

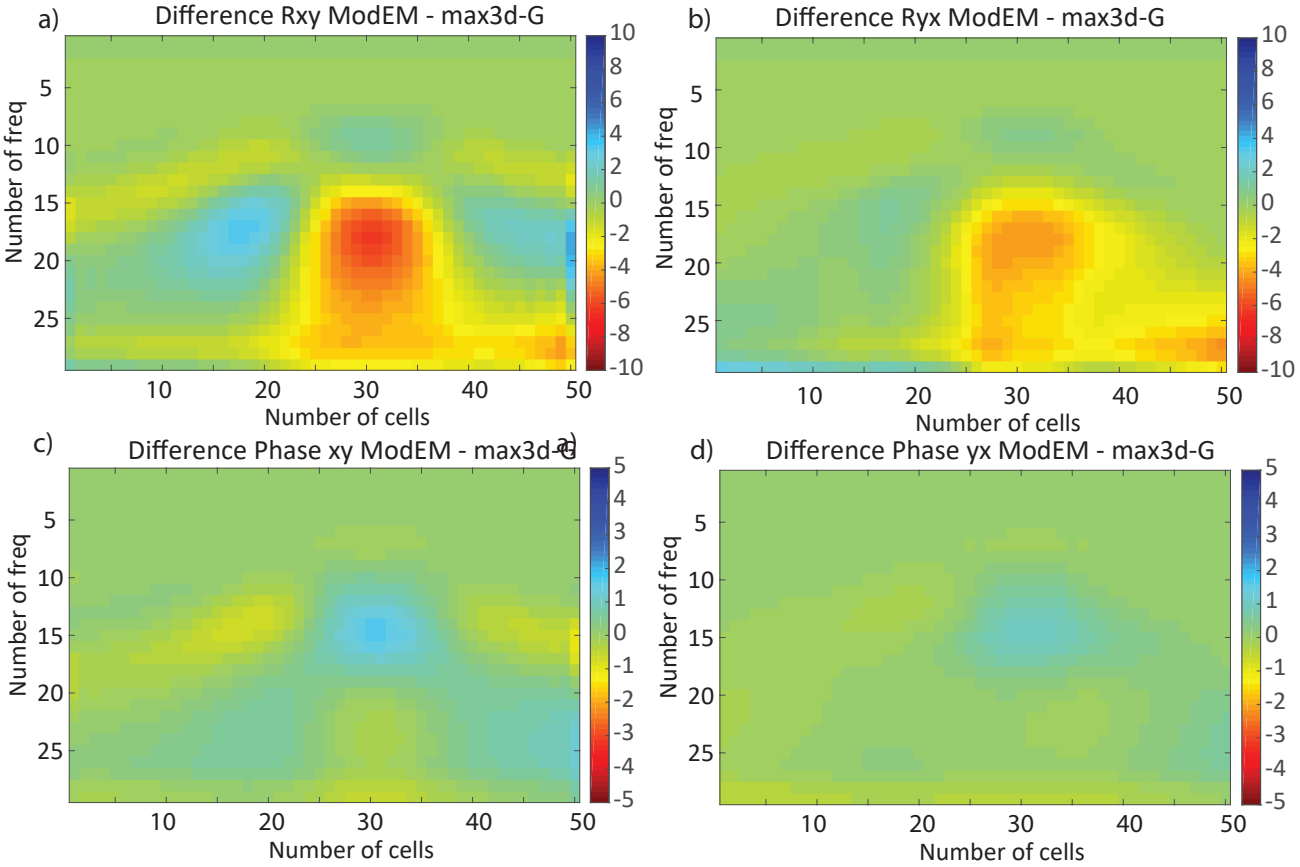

Figure S14. Difference (*ModEM - Max3D-G*) for (a)-(b) apparent resistivity and (c)-(d) phase derived from the off-diagonals components of the impedance tensor.

$$-\frac{d}{dx}\left(k(x)\frac{dT}{dx}\right) = f(x) \tag{1}$$

where the functions $T(x)$, $k(x)$ and $f(x)$ are, respectively, temperature, thermal conductivity and heat source over an interval $[a, b]$. The boundary conditions are temperature at the surface $T(0km) = T_s$ and at the lithosphere-asthenosphere boundary (LAB) $T(150km) = T_{lab}$.

The synthetic data is the heat flux at the surface of the model (Qs) and the unknown parameters are crustal thickness and radioactive heat production (RHP) per unit volume within the crust. The forward problem is solved with the Finite Element method using piecewise linear elements which can be found in:

$https://people.sc.fsu.edu/\sim jburkardt/m\_src/fem1d\_heat\_steady/fem1d\_heat\_steady.html.$

The synthetic data used in the inversion was obtained for a RHP = $1e^{-6}$ W/m^3, Moho depth of 30 km and the constant values shown in Table S2. The resulting Qs for these model parameters is 53.25 mW/m^2. We assumed uncorrelated Gaussian errors with a small standard deviation of 1 mW/m^2.

Table S2: Constant values assumed during the 1D Heat-Transfer inversion.

Surface depth	0 km
Surface temperature	$10°C$
LAB depth	150 km
LAB temperature	$1300°C$
Crust thermal conductivity	2.6 W/mC
Mantle thermal conductivity	3.4 W/mC
Mantle heat production	$2e^{-8}W/m^3$

2.2 Inversion Results

In order to assess the performance of the RB+MCMC algorithm, we ran MCMC inversions using full FE solutions (control/true solution) for all MCMC steps as well as our RB+MCMC algorithm setting different RB tolerances. In all cases, we use a uniform prior defined between 10 and 120 km for Moho depth and between $5e^{-7}$ and $3.5e^{-6}$ W/m^3 for the crustal RHP. The initial model (i.e. starting point in the chain) was located at 50 km - $3.5e^{-6}$ W/m^3. An independence sampler algorithm was used during the inversion (within the bounds given by the prior distribution).

The posterior joint and marginal PDFs obtained after 4,000,000 simulations are shown in Figures S15. The joint distribution exhibits the expected trade-off between crustal thickness and RHP. This highly correlated PDF results from the fact that surface heat flow is mostly sensitive to the amount of heat created inside the model (i.e. to the product of the parameters) and cannot distinguish between these two parameters. We deliberately chose this distribution as it is very challenging for any inversion algorithm. The joint and marginal posterior PDFs of both parameters (moho and CPH) obtained using the RB+MCMC algorithm with $\beta = 1e^{-6}$ (Fig.S15.b) are identical to the posterior PDFs obtained with the full FE MCMC (Fig.S15.a). The total number of bases computed during the 4,000,000 simulations of the RB+MCMC inversion was 40. This number is drastically smaller than the dimensions involved in 4,000,000 FE simulations in the original FE+MCMC inversion, resulting in an efficiency gain of $> 99\%$.

Panels (c)-(f) of Fig.S15 show the results for $\beta = 1e^{-5}$, $\beta = 6e^{-5}$, $\beta = 1e^{-4}$ and $\beta = 1e^{-3}$ with 29, 3, 2 and 1 bases, respectively. Reducing the number of bases to 29 ($\beta = 1e^{-5}$) still produces good representations of the true distribution, although some small differences can be seen in the region around RHP = -5.5. Even in the drastic case of only 3 bases ($\beta = 6e^{-5}$), the high probability regions are still identified, but the PDFs exhibits a clear bias.

The above numerical example clearly demonstrate the effectiveness of our algorithm with an efficiency gain of $> 99\%$ in all cases. An important but expected observation is that the performance of

the RB+MCMC algorithm depends on the choice of the tolerance β. This tolerance is problem dependent and ultimately controls the creation of the bases and the bias between the approximated and the exact PDF.

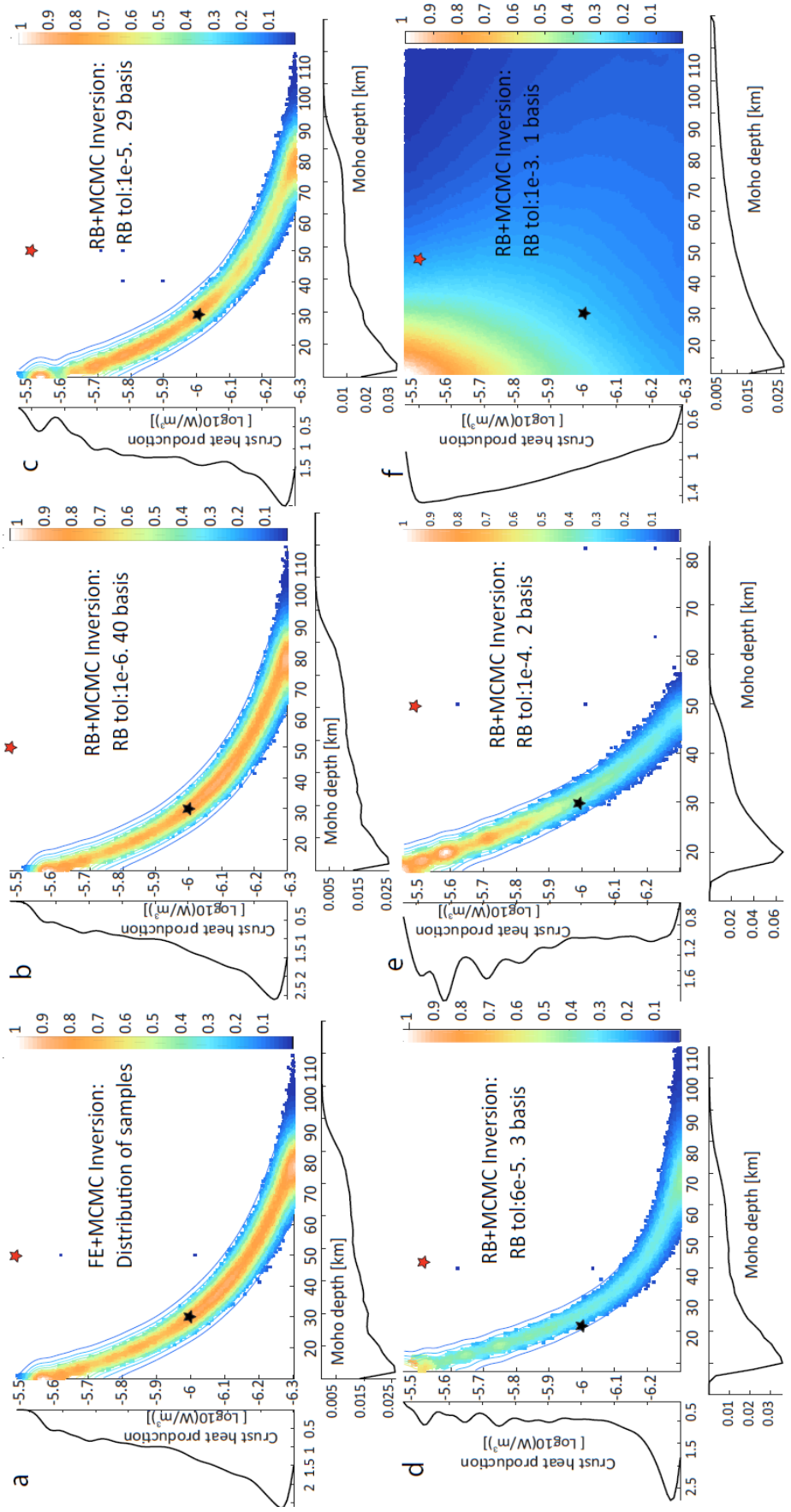

Figure S15. Results for a 2-parameter MCMC inversion. The panels (a)-(f) show the joint and marginal (black solid lines) PDFs. The initial and true models are indicated by red and black stars, respectively. Panel (a) shows the PDFs obtained with full FE (high-fidelity) solutions. Panel (b)-(f) show the PDFs obtained with our RB+MCMC algorithm for RB tolerances of $\beta = 1e^{-6}$, $\beta = 1e^{-5}$, $\beta = 6e^{-5}$, $\beta = 1e^{-4}$ and $\beta = 1e^{-3}$, respectively. The total number of bases computed in each case was 40, 29, 3,2 and 1. In all cases the total number of simulations was 4,000,000.

3 NUMERICAL EXAMPLE 1: ADDITIONAL INVERSION RESULTS

This section shows additional results of the RB+MCMC inversion of the large-scale lithospheric model presented Section 6.2.

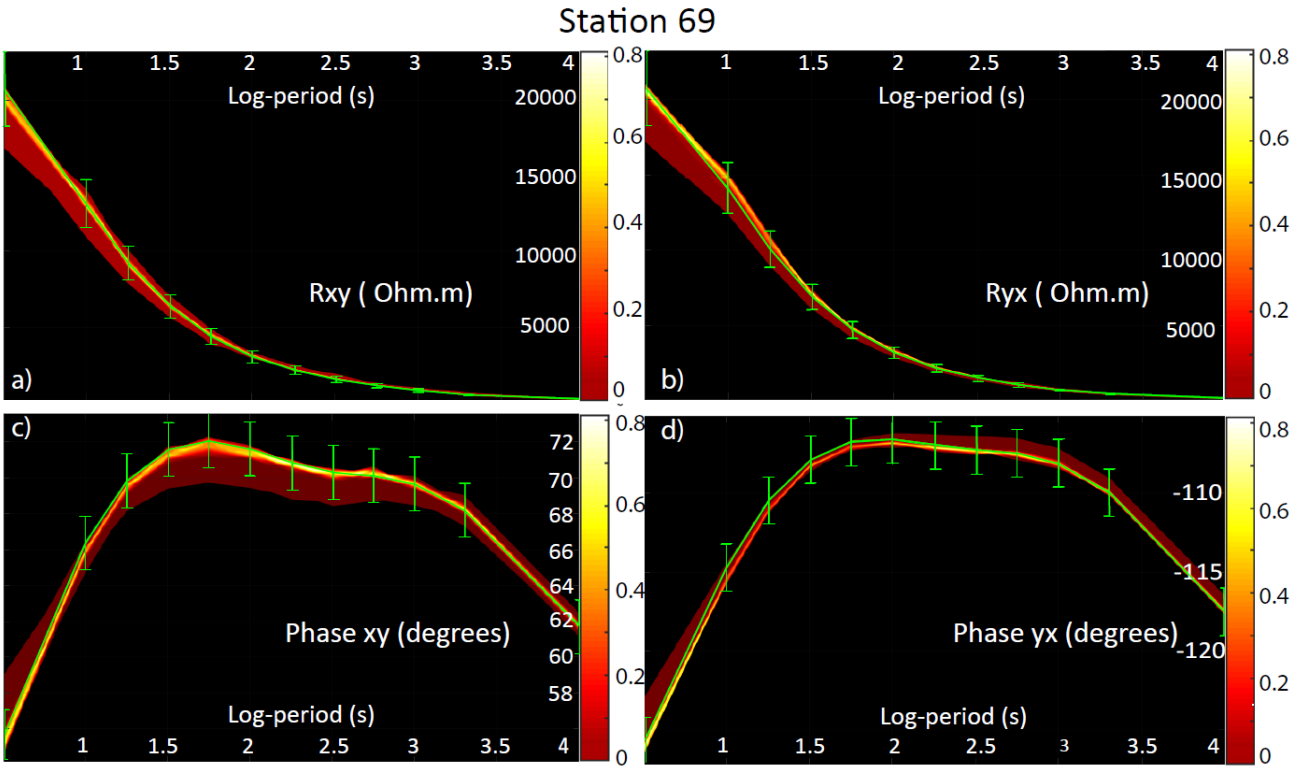

Figure S16. Posterior PDFs of data for station 69. Synthetic data and error bars are plotted in green. (a)-(b) Posterior PDFs of the off-diagonal apparent resistivity. (c)-(d) Posterior PDFs of the off-diagonal apparent phases.

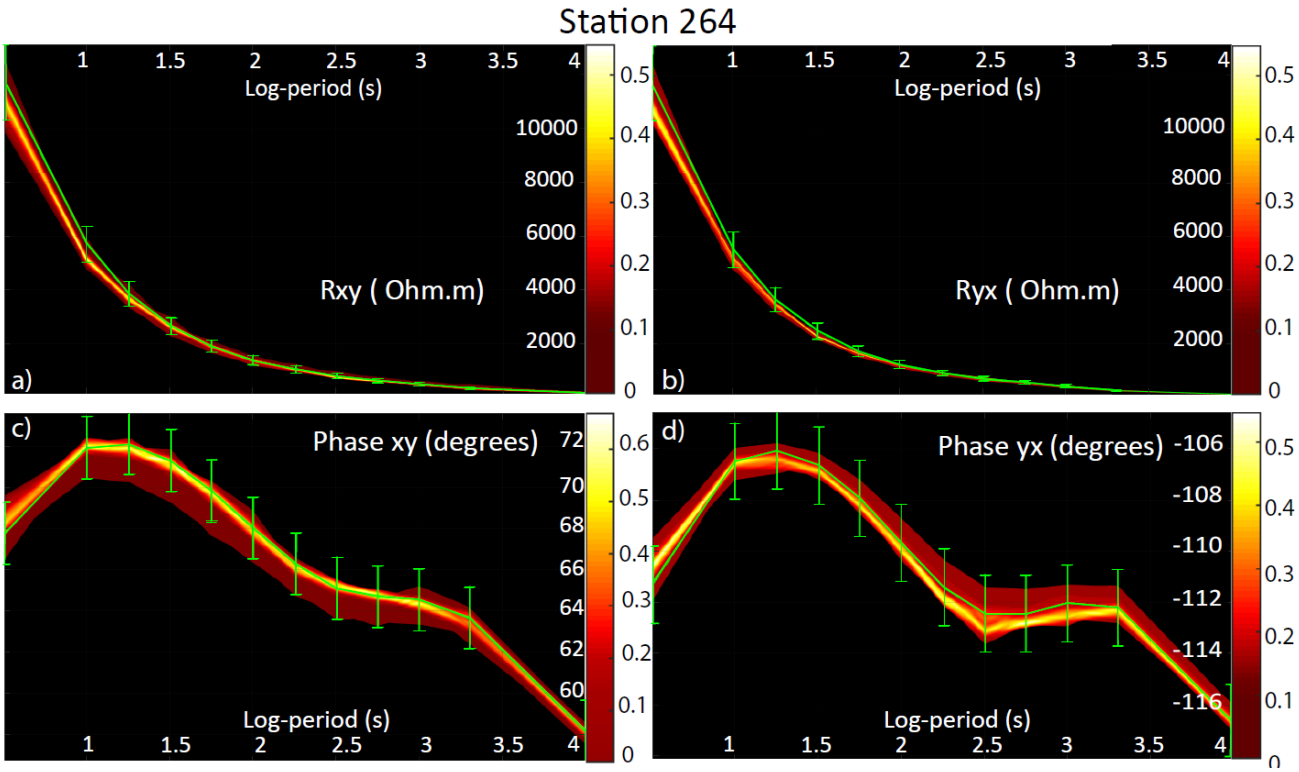

Figure S17. Posterior PDFs of data for station 264. Synthetic data and error bars are plotted in green. (a)-(b) Posterior PDFs of the off-diagonal apparent resistivity. (c)-(d) Posterior PDFs of the off-diagonal apparent phases.

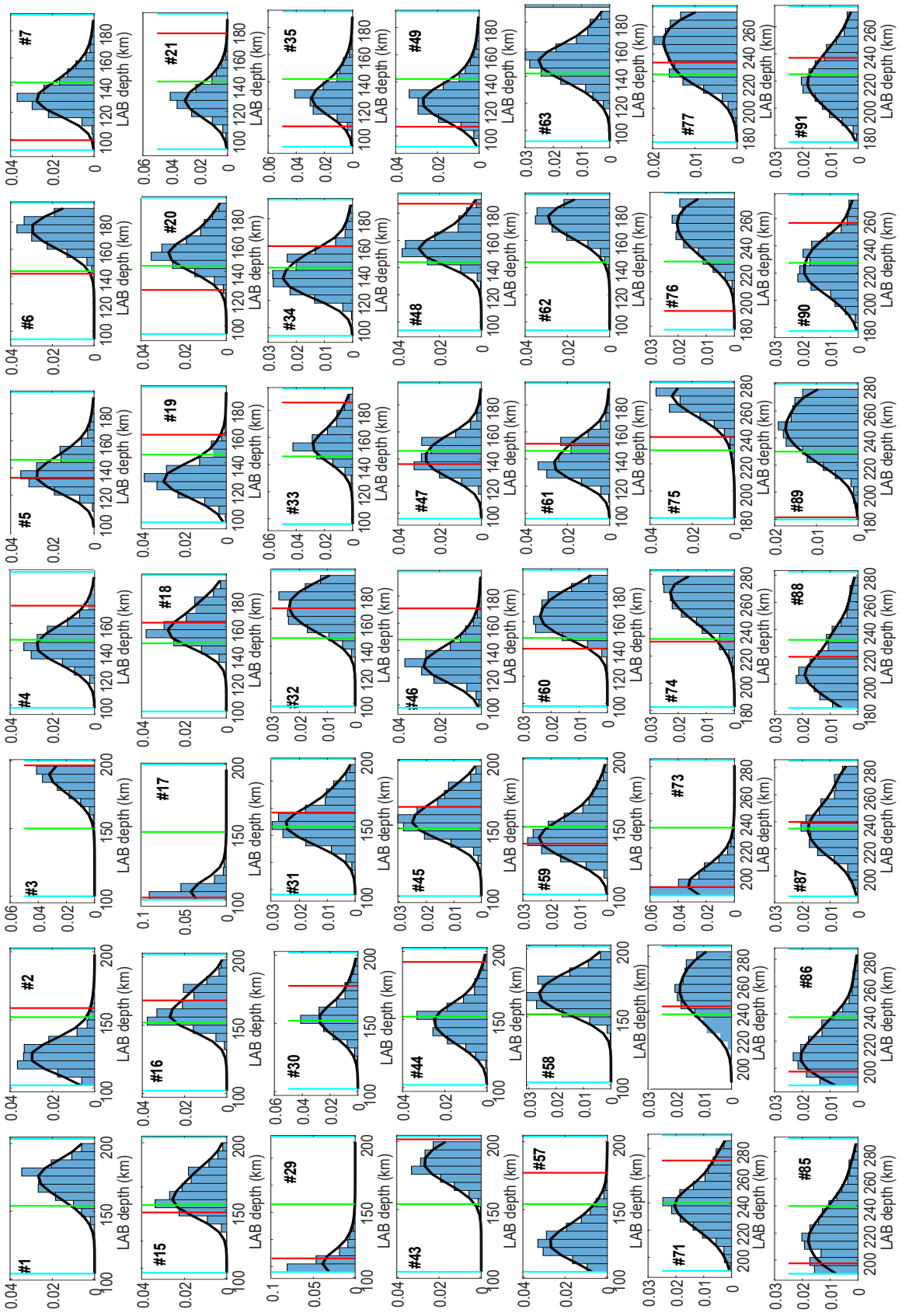

Figure S18. Marginal posterior PDFs (blue bars) and best fitting distributions (black lines) of 49 of the 196 model parameters obtained after 2,500,000 RB+MCMC simulations. The real value, starting value and prior bounds of each parameter are shown in green, red, and light blue vertical lines, respectively. The position of each PDF in the figure corresponds with the location of the 49 columns at the south-west corner of the model (Fig. 1.b in main text).

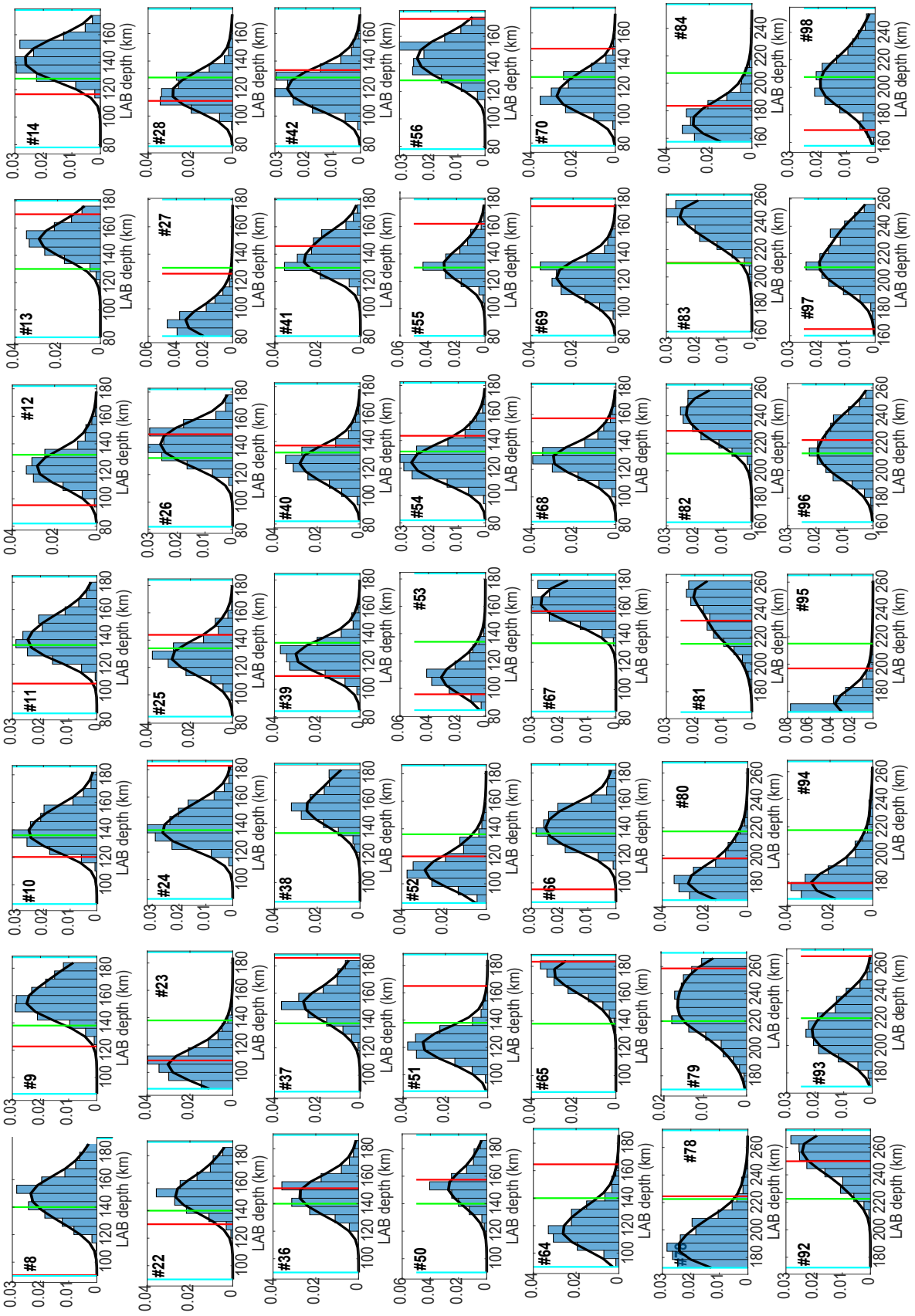

Figure S19. Marginal posterior PDFs (blue bars) and best fitting distributions (black line) of 49 of the 196 model parameters obtained after 2,500,000 RB+MCMC simulations. The real value, starting value and prior bounds of each parameter are shown in green, red, and light blue vertical lines, respectively. The position of each PDF in the figure corresponds with the location of the 49 columns at the north-west corner of the model (Fig. 1.b in main text).

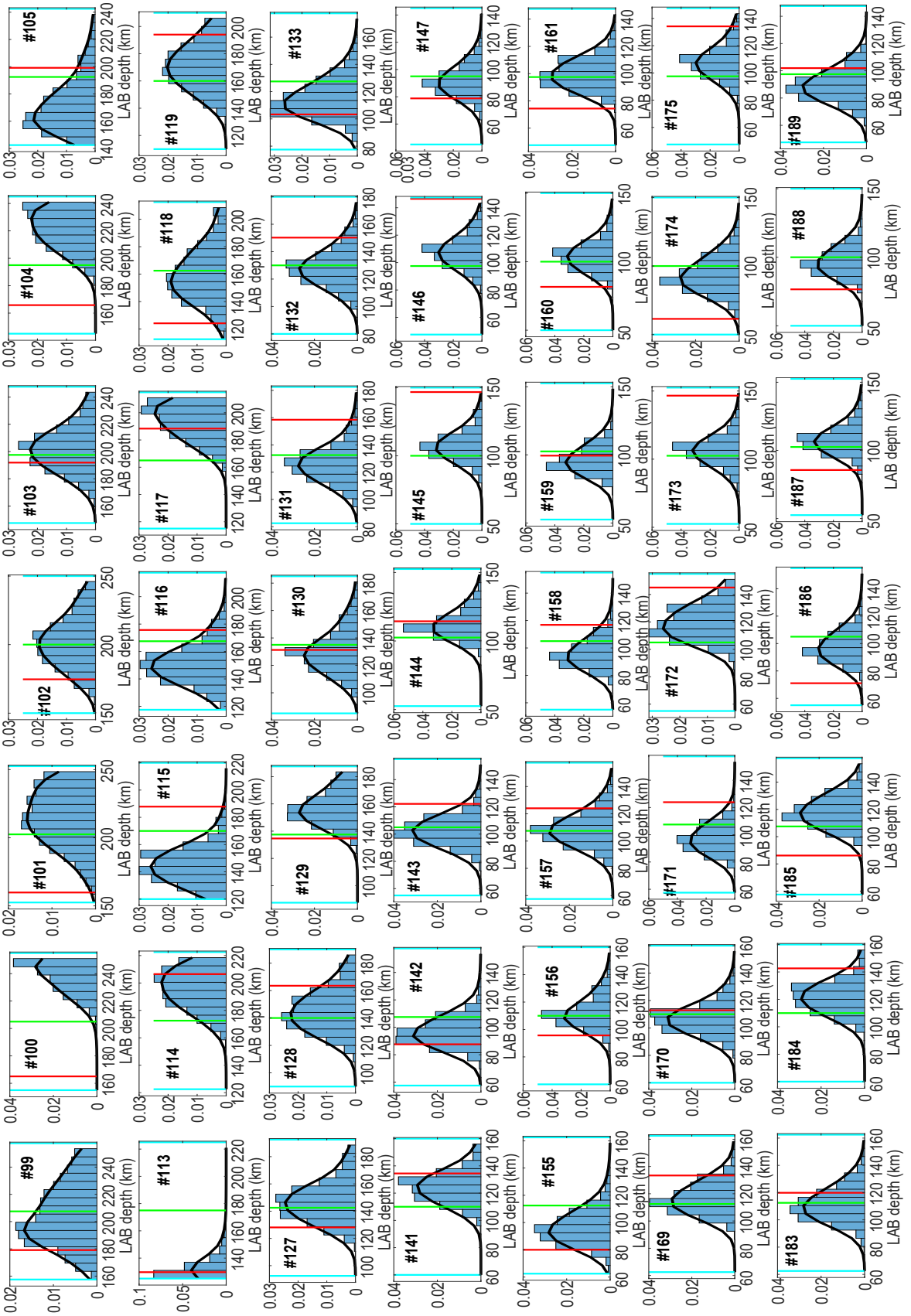

Figure S20. Marginal posterior PDFs (blue bars) and best fitting distributions (black lines) of 49 of the 196 model parameters obtained after 2,500,000 RB+MCMC simulations. The real value, starting value and prior bounds of each parameter are shown in green, red, and light blue vertical lines, respectively. The position of each PDF in the figure corresponds with the location of the 49 columns at the south-east corner of the model (Fig. 1.b in main text).

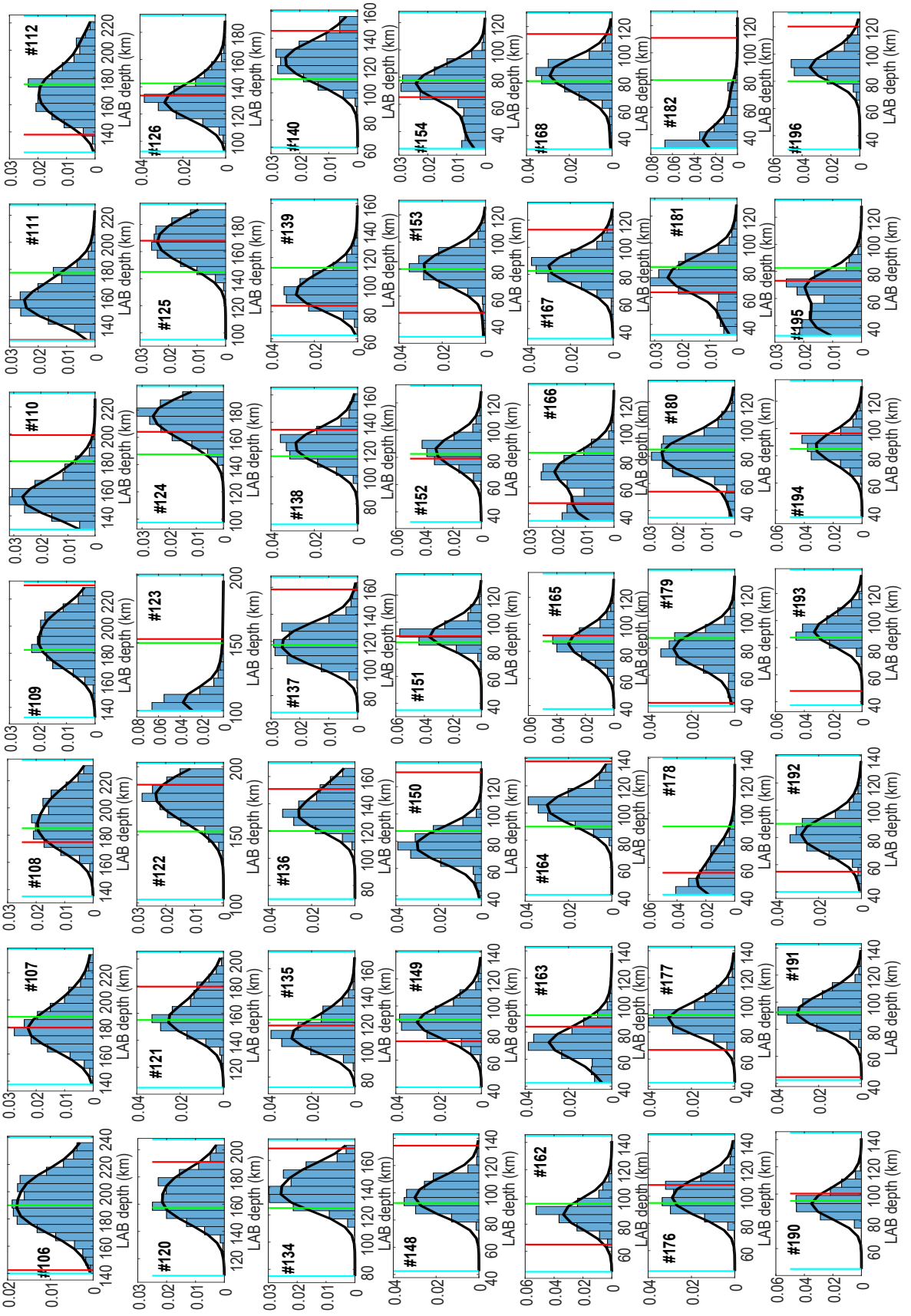

Figure S21. Marginal posterior PDFs (blue bars) and best fitting distributions (black lines) of 49 of the 196 model parameters obtained after 2,500,000 RB+MCMC simulations. The real value, starting value and prior bounds of each parameter are shown in green, red, and light blue vertical lines, respectively. The position of each PDF in the figure corresponds with the location of the 49 columns at the north-east corner of the model (Fig. 1.b in main text).

4 NUMERICAL EXAMPLE 2: ADDITIONAL INVERSION RESULTS

This section shows additional results of the RB+MCMC inversion of the large-scale lithospheric model eith conductivity anomalies presented Section 6.3.

Bibliography

Egbert, G. D. & Kelbert, A., 2012. Computational recipes for electromagnetic inverse problems, *Geophysical Journal International*, **189**(1), 251–267.

Farquharson, C. G., Oldenburg, D. W., Haber, E., & Shekhtman, R., 2002. An algorithm for the three-dimensional inversion of magnetotelluric data, in *SEG Technical Program Expanded Abstracts 2002*, pp. 649–652, Society of Exploration Geophysicists.

Mackie, R. L., Smith, J. T., & Madden, T. R., 1994. Three-dimensional electromagnetic modeling using finite difference Equations: The magnetotelluric example, *Radio Science*, **29**(4), 923–935.

Miensopust, M. P., Queralt, P., Jones, A. G., & modellers, D. M., 2013. Magnetotelluric 3-D inversion—a review of two successful workshops on forward and inversion code testing and comparison, *Geophysical Journal International*, **193**(3), 1216–1238.

Nam, M. J., Kim, H. J., Song, Y., Lee, T. J., Son, J.-S., & Suh, J. H., 2007. 3D magnetotelluric modelling including surface topography, *Geophysical Prospecting*, **55**(2), 277–287.

Sheen, D., 1997. Approximation of electromagnetic fields: Part I. Continuous problems, *SIAM Journal on Applied Mathematics*, **57**(6), 1716–1736.

Siripunvaraporn, W., Egbert, G., & Lenbury, Y., 2002. Numerical accuracy of magnetotelluric modeling: a comparison of finite difference approximations, *Earth, planets and space*, **54**(6), 721–725.

Zyserman, F. I. & Santos, J. E., 2000. Parallel finite element algorithm with domain decomposition for three-dimensional magnetotelluric modelling, *Journal of Applied Geophysics*, **44**(4), 337–351.

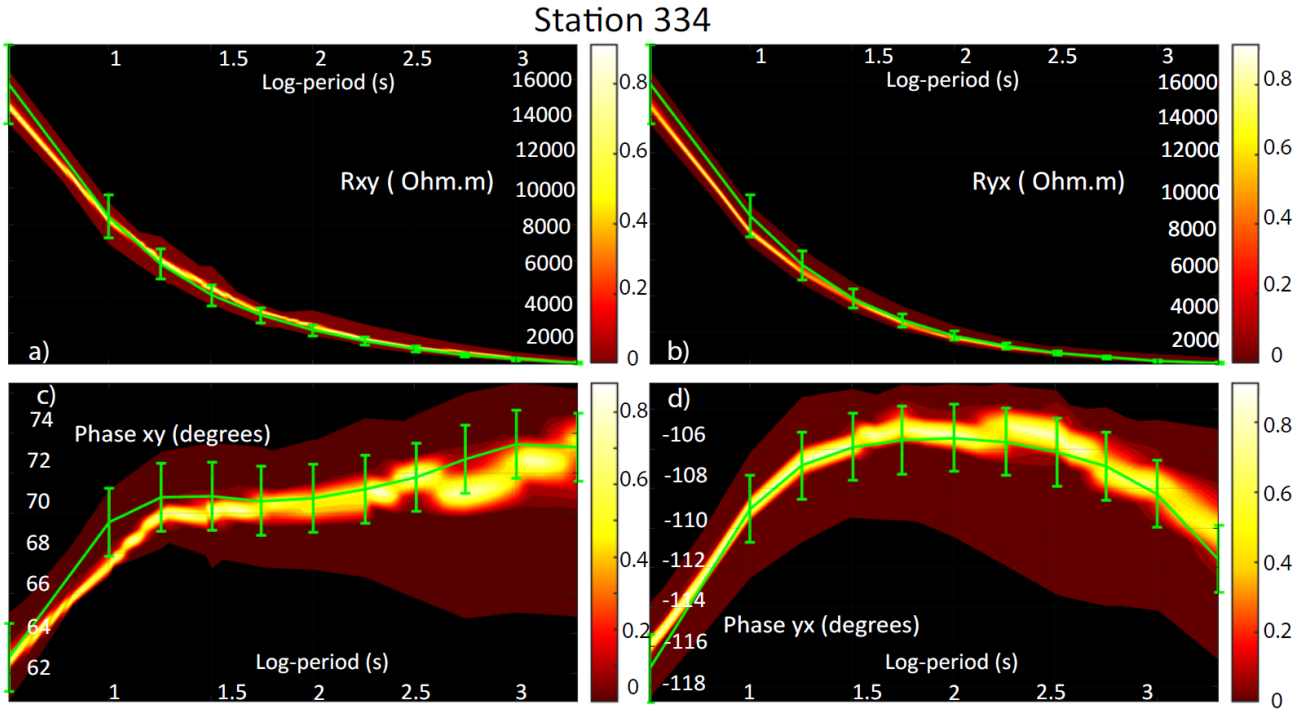

Figure S22. Posterior PDFs of data for station 334. Synthetic data and error bars are plotted in green. (a)-(b) Posterior PDFs of the off-diagonal apparent resistivity. (c)-(d) Posterior PDFs of the off-diagonal apparent phases.

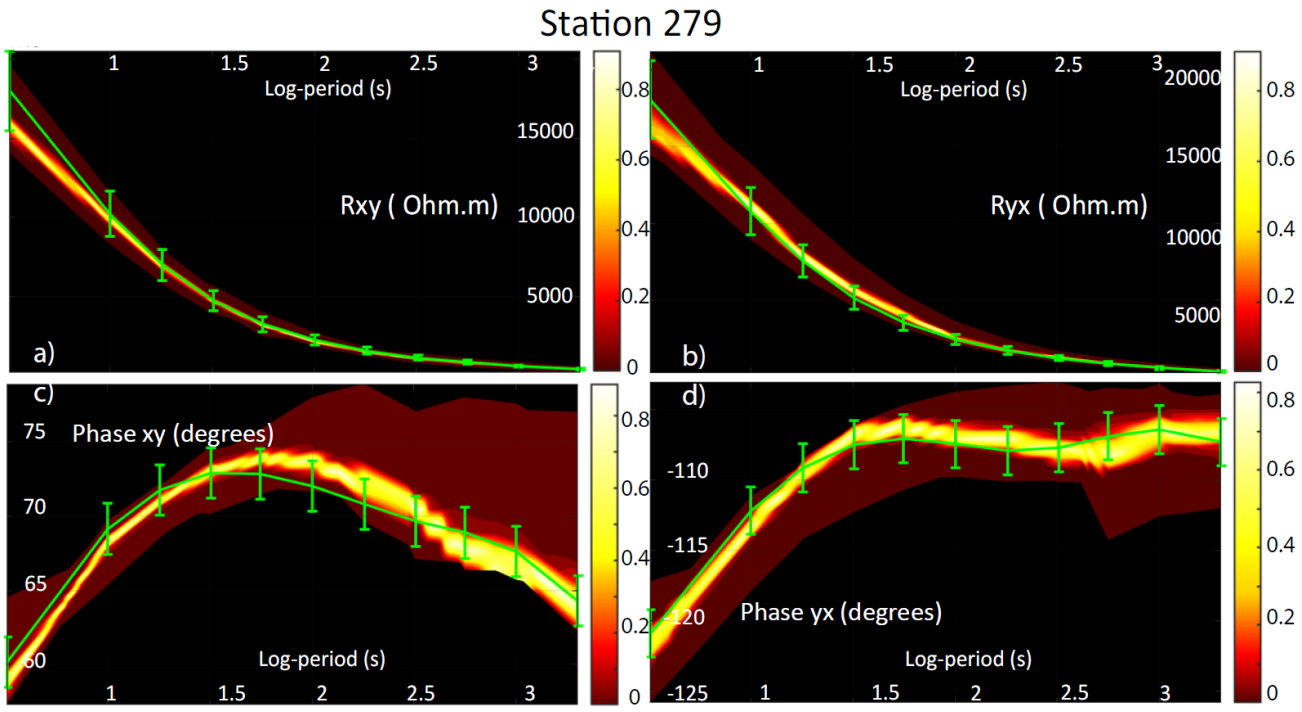

Figure S23. Posterior PDFs of data for station 279. Synthetic data and error bars are plotted in green. (a)-(b) Posterior PDFs of the off-diagonal apparent resistivity. (c)-(d) Posterior PDFs of the off-diagonal apparent phases.

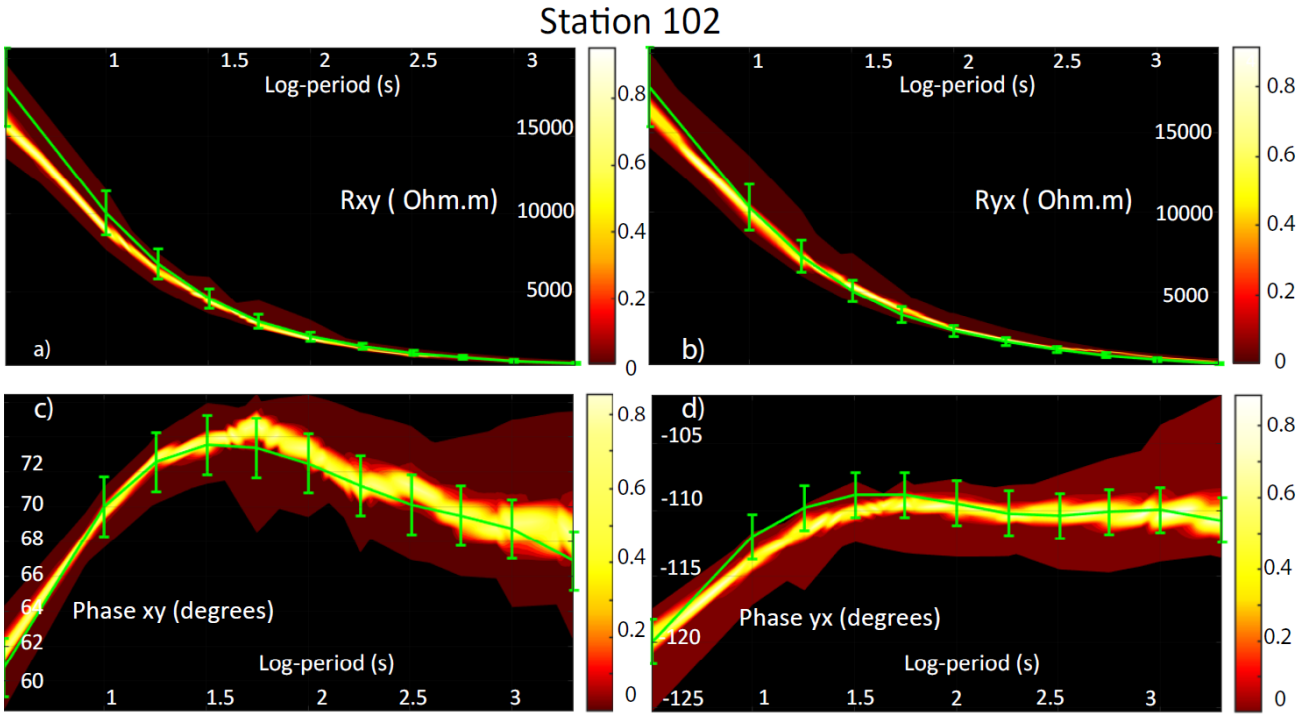

Figure S24. Posterior PDFs of data for station 102. Synthetic data and error bars are plotted in green. (a)-(b) Posterior PDFs of the off-diagonal apparent resistivity. (c)-(d) Posterior PDFs of the off-diagonal apparent phases.

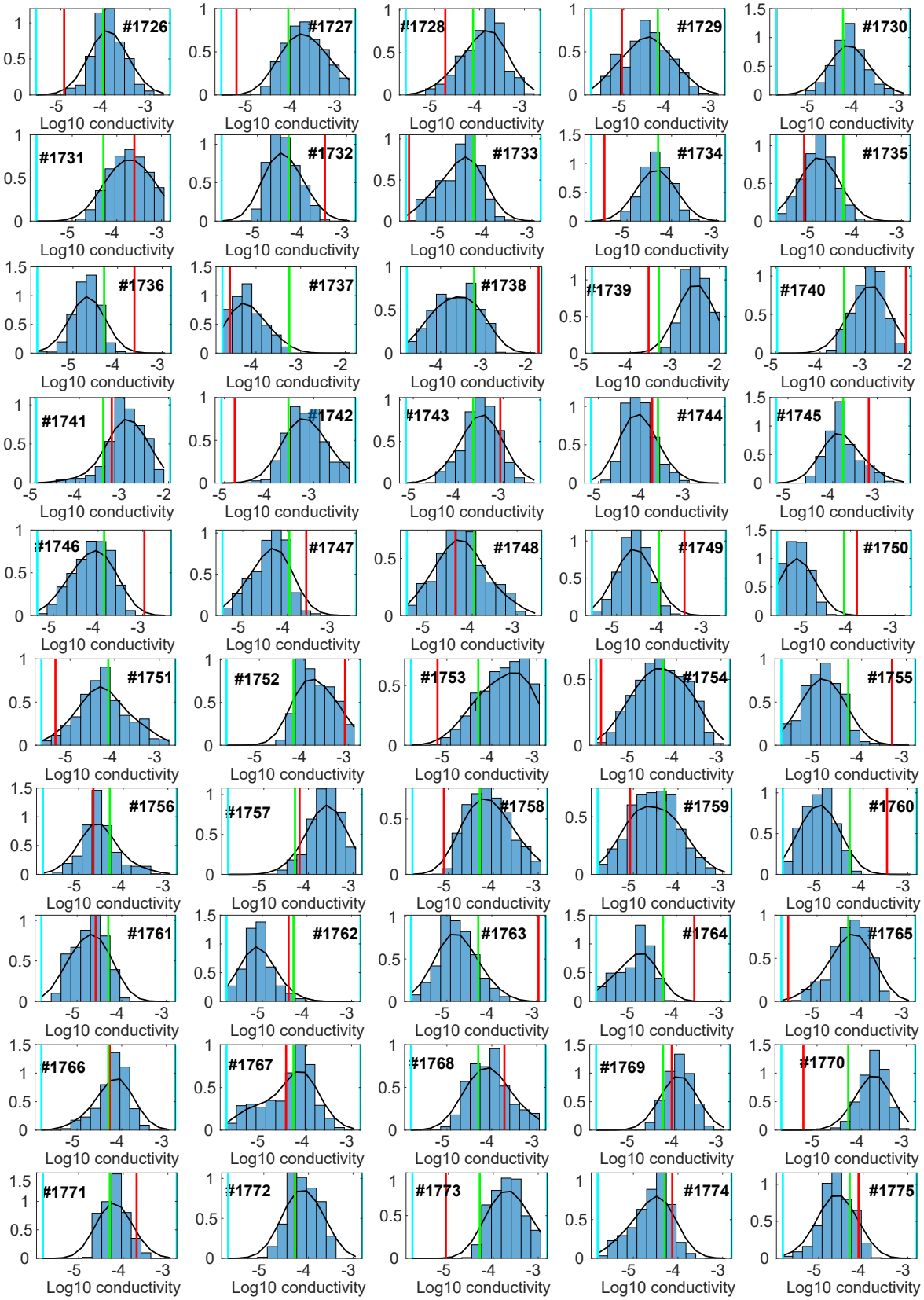

Figure S25. Marginal posterior PDFs (blue bars) and best fitting distributions (black lines) of 50 of the 1782 node-parameters obtained after 2,500,000 RB+MCMC simulations. The real value, starting value and prior bounds of each parameter are shown in green, red, and light blue vertical lines, respectively.

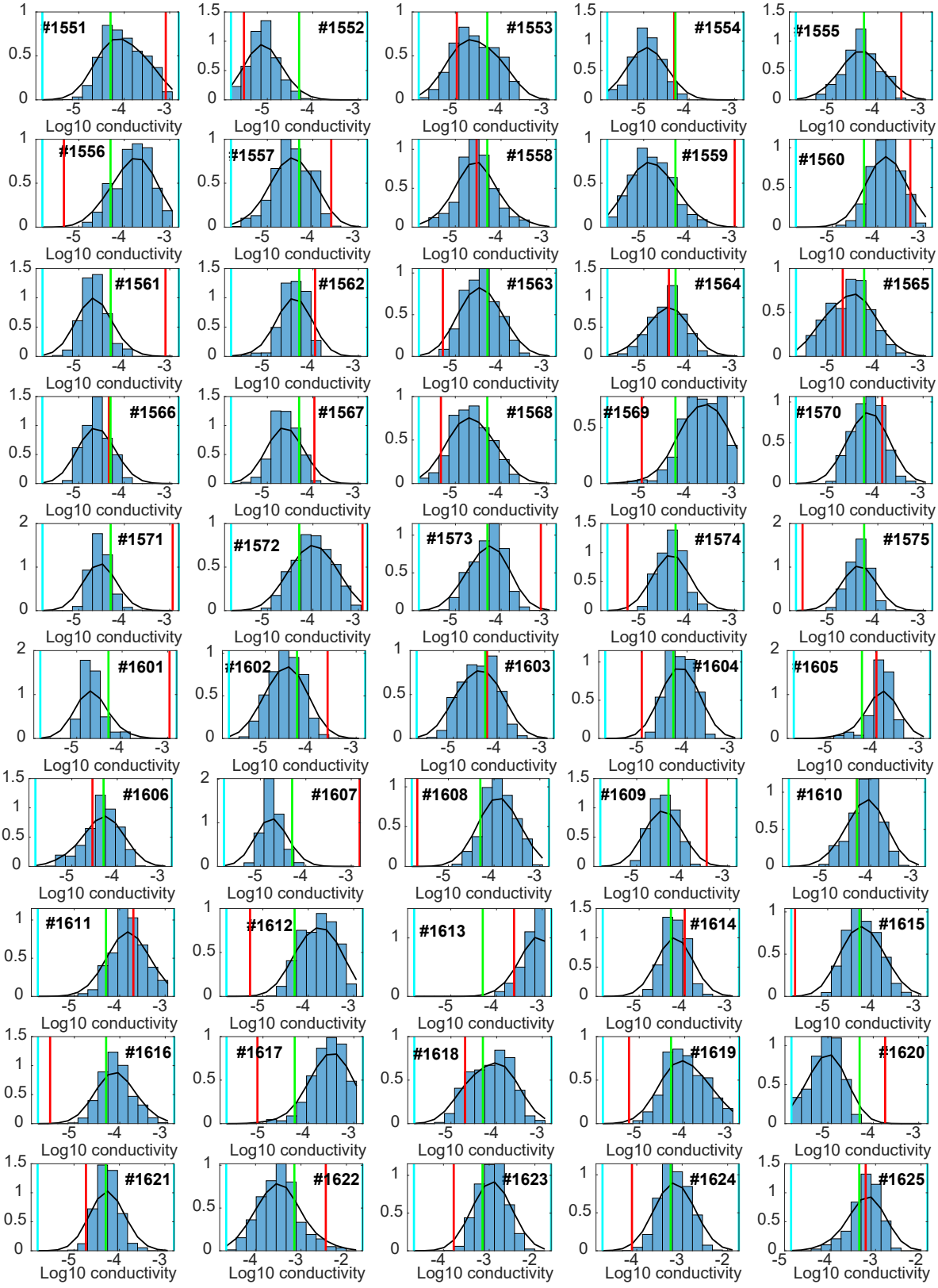

Figure S26. Marginal posterior PDFs (blue bars) and best fitting distributions (black lines) of 50 of the 1782 node-parameters obtained after 2,500,000 RB+MCMC simulations. The real value, starting value and prior bounds of each parameter are shown in green, red, and light blue vertical lines, respectively.